



**Synchronization and alignment of model oscillators based on Quincke rotation**Zhengyan Zhang  and Kyle J. M. Bishop \**Department of Chemical Engineering, Columbia University, New York, New York 10027, USA*

(Received 4 February 2023; accepted 4 April 2023; published 22 May 2023)

Colloidal spheres in weakly conductive fluids roll back and forth across the surface of a plane electrode when subject to strong electric fields. The so-called Quincke oscillators provide a basis for active matter based on self-oscillating units that can move, align, and synchronize within dynamic particle assemblies. Here, we develop a dynamical model for oscillations of a spherical particle and investigate the coupled dynamics of two such oscillators in the plane normal to the field. Building on existing descriptions of Quincke rotation, the model describes the dynamics of the charge, dipole, and quadrupole moments due to charge accumulation at the particle-fluid interface and particle rotation in the external field. The dynamics of the charge moments are coupled by the addition of a conductivity gradient, which describes asymmetries in the rates of charging near the electrode. We study the behavior of this model as a function of the field strength and gradient magnitude to identify the conditions required for sustained oscillations. We investigate the dynamics of two neighboring oscillators coupled by far field electric and hydrodynamic interactions in an unbounded fluid. Particles prefer to align and synchronize their rotary oscillations along the line of centers. The numerical results are reproduced and explained by accurate low-order approximations of the system dynamics based on weakly coupled oscillator theory. The coarse-grained dynamics of the oscillator phase and angle can be used to investigate collective behaviors within ensembles of many self-oscillating colloids.

DOI: [10.1103/PhysRevE.107.054603](https://doi.org/10.1103/PhysRevE.107.054603)**I. INTRODUCTION**

Collections of mobile oscillators can exhibit complex behaviors due to interactions that influence and respond to their respective positions and phases [1]. These “swarmalators” combine the swarming dynamics of mobile agents with the synchronization of coupled oscillators to produce new forms of self-organization outside of equilibrium. In addition to their positions and orientations, mobile oscillators are distinguished by internal states, namely, the oscillation phase, that influence their interactions with neighboring oscillators. In general, these interactions are nonreciprocal such that the action of one oscillator on another does not produce an equal and opposite reaction [2]. As a result, weakly coupled oscillators can beat faster (or slower) when synchronized due to interactions between their respective phases. Similar effects drive steady currents among swarmalators that break time-reversal symmetry to enable diverse behaviors prohibited at equilibrium [3].

Active colloidal particles [4] powered by chemical fuels [5,6] or external fields [7,8] enable experimental models of mobile oscillators by which to investigate their collective behaviors [9]. Magnetic Janus spheres with anisotropic susceptibility exhibit simultaneous rotation and oscillation in a precessing field that mediate their synchronization and self-assembly [10]. Conductive particles oscillating between biased electrodes by contact-charge electrophoresis (CCEP)

attract or repel each other depending on their relative phases [11,12]. Pear-shaped colloids rolling along circular trajectories by Quincke rotation organize to form aster-like vortices and rotating flocks characterized by sustained particle currents [13]. In these examples, the oscillatory dynamics of each individual particle is coupled to that of its neighbors by magnetic [10,14], electric [11,12], and/or hydrodynamic [15,16] interactions. The oscillator positions and phases evolve in time due to nonreciprocal interactions that cannot be described by gradients of a scalar potential.

Recently, we reported a colloidal oscillator based on Quincke rotation [17] of a spherical particle at the surface of a plane electrode [18] (Fig. 1). Like similar Quincke rollers [19,20], particle rotation is caused by charge accumulation at the particle-fluid interface and its mechanical relaxation in the applied field. Oscillatory dynamics at high field strengths is attributed to asymmetries in the rates of charging that occur when the particle size is commensurate with a field-induced boundary layer near the electrode surface. The back-and-forth motion of particles is reproduced by a modified leaky dielectric model [21,22] that uses spatial gradients in the fluid conductivity to describe the effects of asymmetric charging. Notably, Quincke oscillators produce electric and hydrodynamic disturbances that can influence the dynamics of neighboring particles; however, the effects of these interactions on the oscillation phase and orientation have not been investigated. Unlike similar interactions between spherical particles under Quincke rotation [23,24], coupled particle oscillators can both synchronize and align to enable new types of collective behavior.

\*kyle.bishop@columbia.edu

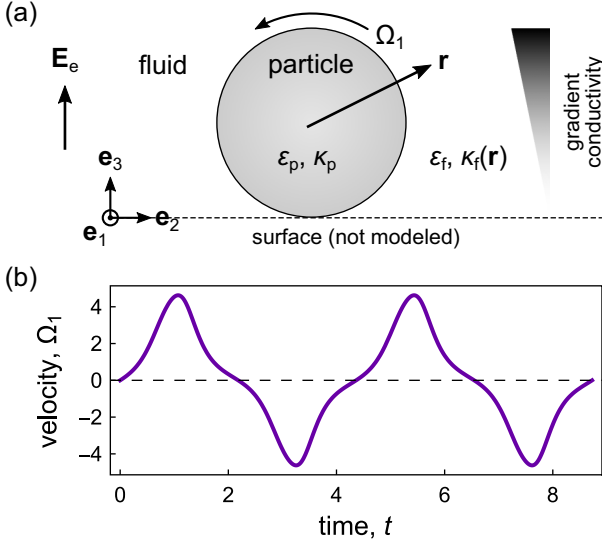


FIG. 1. (a) Schematic illustration of a single spherical particle of radius  $a$ , permittivity  $\epsilon_p$ , and conductivity  $\kappa_p$  immersed in a viscous fluid of permittivity  $\epsilon_f$  and conductivity  $\kappa_f(\mathbf{r})$ . Different from the standard model of Quincke rotation, we consider the effects of conductivity gradients  $\nabla\kappa_f \neq 0$ , which describe asymmetric rates of charge accumulation at the particle surface [18]. Under appropriate conditions, application of an external field  $\mathbf{E}_e$  causes the particle to rotate back and forth about an axis perpendicular to the field. (b) Oscillatory dynamics of the angular velocity  $\Omega_1$  as predicted by the model for (dimensionless) parameters  $\epsilon_p = 1.5$ ,  $\kappa_p = 0$ ,  $E_e = 10$ ,  $\gamma = 1.2$ . All quantities are presented using natural units described in the text.

Here, we develop a dynamical model for Quincke oscillation of a spherical particle and investigate the coupled dynamics of two model oscillators in the plane normal to the field. Building on previous work on Quincke rotation [23,24], the model uses the leaky dielectric framework to describe the dynamics of the charge moments up to the quadrupole. The addition of a conductivity gradient parallel to the applied field leads to new couplings between the moments that drive particle oscillations at high field strengths. We characterize the behaviors predicted by the model for different field strengths and gradient magnitudes. To describe the coupled dynamics of two oscillators, we consider the leading-order electric and hydrodynamic interactions in the far field. Numerical integration of the model suggests that these interactions act to synchronize and align particle rotation parallel to the line of centers. Using the theory of weakly coupled oscillators [25,26], we derive accurate low-order approximations of the system dynamics to describe the evolution of the oscillator angles and phases. These coarse-grained models can be used to investigate the collective dynamics of oscillator ensembles comprised of many self-oscillating colloids.

## II. QUINCKE OSCILLATOR MODEL

Building on existing models of Quincke rotation [23,24], we develop a simple model to describe the Quincke oscillations of a spherical particle subject to an external field. Quincke rotation is well described by the Taylor-Melcher leaky dielectric model [21,22], which treats the particle and

the surrounding fluid as homogeneous Ohmic conductors containing no free charge. The application of an external field drives the accumulation of charge at the particle-fluid interface. Above a critical field strength, the action of the field on the field-induced surface charge causes the particle to rotate at a steady rate. To induce oscillations, we introduce a gradient in the fluid conductivity oriented parallel to the applied field such that charge accumulates faster on one side of the particle and slower on the other. This asymmetric charging process provides a crude approximation to the more complex processes of charge carrier formation and recombination near the electrode surface [18]. For simplicity, our model ignores other effects of the electrode such as enhancements in the hydrodynamic resistance to rotation and electrostatic interactions with the particle's image. With these simplifying assumptions, we derive evolution equations for the particle charge  $q$ , dipole  $\mathbf{p}$ , and quadrupole  $\mathbf{Q}$  moments, which are coupled to one another by the gradient conductivity. Interactions with higher-order charge moments are neglected.

We consider a spherical particle of radius  $a$ , permittivity  $\epsilon_p$ , and conductivity  $\kappa_p$  immersed in an unbounded fluid of permittivity  $\epsilon_f$  and conductivity  $\kappa_f(\mathbf{r})$  (Fig. 1). Assuming zero charge in each bulk phase, the electric potential inside and outside of the sphere are governed by the Laplace equation

$$\begin{aligned} \nabla^2 \bar{\varphi} &= 0 & \text{for } r < a, \\ \nabla^2 \varphi &= 0 & \text{for } r > a. \end{aligned} \quad (1)$$

Consequently, the potentials can be expanded in multipole expansions of the form

$$\begin{aligned} \bar{\varphi}(\mathbf{r}) &= \varphi_e(\mathbf{r}) + \frac{q}{a} + \frac{\mathbf{r} \cdot \mathbf{p}}{a^3} + \frac{1}{2} \frac{\mathbf{r} \mathbf{r} : \mathbf{Q}}{a^5} + \dots & \text{for } r < a, \\ \varphi(\mathbf{r}) &= \varphi_e(\mathbf{r}) + \frac{q}{r} + \frac{\mathbf{r} \cdot \mathbf{p}}{r^3} + \frac{1}{2} \frac{\mathbf{r} \mathbf{r} : \mathbf{Q}}{r^5} + \dots & \text{for } r > a, \end{aligned} \quad (2)$$

where  $\varphi_e(\mathbf{r})$  is the external potential present in the particle's absence. At the particle surface, the charge density  $\sigma$  is related to the jump in the electric displacement field as

$$\sigma = -\hat{\mathbf{r}} \cdot (\epsilon_f \nabla \varphi - \epsilon_p \nabla \bar{\varphi}) \quad \text{for } r = a, \quad (3)$$

where  $\hat{\mathbf{r}}$  is the unit vector in the radial direction. The surface charge density evolves in time due to the jump in the electric current normal to the particle-fluid interface and to the rotation of the particle with angular velocity  $\boldsymbol{\Omega}$

$$\frac{\partial \sigma}{\partial t} - \hat{\mathbf{r}} \cdot (\kappa_f(\mathbf{r}) \nabla \varphi - \kappa_p \nabla \bar{\varphi}) + \nabla_s \cdot (\sigma \boldsymbol{\Omega} \times \mathbf{r}) = 0. \quad (4)$$

Here, we deviate from the standard treatment of Quincke rotation with the introduction of a position-dependent conductivity  $\kappa_f(\mathbf{r})$ . With this change, the leaky-dielectric model is no longer self-consistent: steady currents through a medium of variable conductivity are accompanied by volumetric charge, which is neglected in Eq. (1). This heuristic approximation is motivated by the asymmetric charging of the particle surface when its size is comparable to that of a field-induced boundary layer at the electrode surface [18].

As described previously [23,24] and detailed in the Supplemental Material [32], we derive the moment evolution equations by substituting the multipole expansion into Eq. (4)

for the surface charge and collecting like powers of  $\mathbf{r}$ . The charge  $q$ , dipole  $\mathbf{p}$ , and quadrupole  $\mathbf{Q}$  evolve in time as

$$\frac{dq}{dt} = -\frac{1}{\tau}q - \frac{\boldsymbol{\gamma}}{\tau} \cdot \left( \frac{2}{3a}\mathbf{p} - \frac{a^2}{3}\nabla\varphi_e(\mathbf{0}) \right), \quad (5)$$

$$\begin{aligned} \frac{d\mathbf{p}}{dt} = & \boldsymbol{\Omega} \times [\mathbf{p} + a^3\epsilon'_{\text{cm}}\nabla\varphi_e(\mathbf{0})] - \frac{1}{\tau'}[\mathbf{p} + a^3\kappa'_{\text{cm}}\nabla\varphi_e(\mathbf{0})] \\ & - \frac{\boldsymbol{\gamma}'}{\tau'} \cdot \left( aq\boldsymbol{\delta} + \frac{3}{5a}\mathbf{Q} - \frac{2a^4}{5}\nabla\nabla\varphi_e(\mathbf{0}) \right), \end{aligned} \quad (6)$$

$$\begin{aligned} \frac{d\mathbf{Q}}{dt} = & \{ \boldsymbol{\Omega} \times [2\mathbf{Q} + 4a^5\epsilon''_{\text{cm}}\nabla\nabla\varphi_e(\mathbf{0})] \}^{\text{st}} \\ & - \frac{1}{\tau''}(\mathbf{Q} + 2a^5\kappa''_{\text{cm}}\nabla\nabla\varphi_e(\mathbf{0})) \\ & - \frac{1}{\tau''}\{\boldsymbol{\gamma}''[4a\mathbf{p} - 2a^4\nabla\varphi_e(\mathbf{0})]\}^{\text{st}}. \end{aligned} \quad (7)$$

Here, the timescales for the relaxation of the charge, dipole, and quadrupole are, respectively,

$$\tau = \frac{\epsilon_f}{\kappa_f(\mathbf{0})}, \quad \tau' = \frac{\epsilon_p + 2\epsilon_f}{\kappa_p + 2\kappa_f(\mathbf{0})}, \quad \tau'' = \frac{2\epsilon_p + 3\epsilon_f}{2\kappa_p + 3\kappa_f(\mathbf{0})}. \quad (8)$$

Similarly, the dimensionless conductivity gradients are

$$\boldsymbol{\gamma} = \frac{a\nabla\kappa_f(\mathbf{0})}{\kappa_f(\mathbf{0})}, \quad \boldsymbol{\gamma}' = \frac{a\nabla\kappa_f(\mathbf{0})}{\kappa_p + 2\kappa_f(\mathbf{0})}, \quad \boldsymbol{\gamma}'' = \frac{a\nabla\kappa_f(\mathbf{0})}{2\kappa_p + 3\kappa_f(\mathbf{0})}. \quad (9)$$

The Clausius-Mossotti factors for the dipole and quadrupole are

$$\begin{aligned} \epsilon'_{\text{cm}} &= \frac{\epsilon_p - \epsilon_f}{\epsilon_p + 2\epsilon_f}, & \epsilon''_{\text{cm}} &= \frac{\epsilon_p - \epsilon_f}{2\epsilon_p + 3\epsilon_f} \\ \kappa'_{\text{cm}} &= \frac{\kappa_p - \kappa_f(\mathbf{0})}{\kappa_p + 2\kappa_f(\mathbf{0})}, & \kappa''_{\text{cm}} &= \frac{\kappa_p - \kappa_f(\mathbf{0})}{2\kappa_p + 3\kappa_f(\mathbf{0})}. \end{aligned} \quad (10)$$

To preserve the properties of the quadrupole, which is symmetric and traceless, the bracketed terms with superscript ‘‘st’’ denote the symmetric and traceless components of the second-order tensor, that is,  $[\mathbf{A}]^{\text{st}} = \frac{1}{2}(\mathbf{A} + \mathbf{A}^{\text{T}}) - \frac{1}{3}\text{tr}(\mathbf{A})\boldsymbol{\delta}$ , where  $\mathbf{A}^{\text{T}}$  denotes the transpose,  $\boldsymbol{\delta}$  is the identity tensor, and  $\text{tr}(\mathbf{A}) = A_{ii}$  denotes the trace. Equation (7) neglects the additional contributions due to the octopole, thereby closing an otherwise infinite system of moment equations in which the conductivity gradient couples the dynamics of neighboring moments. The validity of this approximation is established by comparison to the full numeric solution for different gradient magnitudes  $\gamma$  (see Supplemental Material, Sec. 2 [32]).

To determine the angular velocity  $\boldsymbol{\Omega}$  of particle rotation, we balance the electrostatic torque [27] on the particle in the external electric field with the hydrodynamic torque [28] on the particle in the ambient flow field  $\mathbf{u}_e(\mathbf{r})$  at low Reynolds number

$$\begin{aligned} 8\pi\eta a^3[\boldsymbol{\Omega} - \frac{1}{2}\nabla \times \mathbf{u}_e(\mathbf{0})] = & -4\pi\epsilon_f[\mathbf{p} \times \nabla\varphi_e(\mathbf{0}) \\ & + \frac{1}{3}(\mathbf{Q} \cdot \nabla) \times \nabla\varphi_e(\mathbf{0})], \end{aligned} \quad (11)$$

where  $\eta$  is the fluid viscosity. On the right-hand side, the expression for the electric torque neglects additional contributions due to higher-order moments and their interactions with higher-order gradients of the external field. For the purpose of calculation, the quadrupolar contribution to the torque can

be written using index notation as  $\frac{1}{3}\epsilon_{ijk}Q_{jl}\partial_{x_i}\partial_{x_k}\varphi_e(\mathbf{0})$ . On the left-hand side, the expression for the hydrodynamic torque assumes that the spherical particle is immersed in an unbounded fluid. The torque balance (11) omits the effect of particle inertia, which is assumed to be negligible for micron scale particles [18].

To facilitate our analysis, we adopt a convenient set of units in which the following quantities are set to 1: the particle radius  $a$ , the fluid permittivity  $\epsilon_f$ , the fluid conductivity  $\kappa_f(\mathbf{0})$ , and the fluid viscosity  $\eta$ . In these units, length is scaled by the radius  $a$ , time by  $\epsilon_f/\kappa_f(\mathbf{0})$ , the electric field by  $E_s = \sqrt{\eta\kappa_f(\mathbf{0})/\epsilon_f^2}$ , the particle charge by  $a^2E_s$ , the dipole by  $a^3E_s$ , and the quadrupole by  $a^4E_s$ . We use the same notation to denote the resulting dimensionless variables. The dimensionless problem is fully specified by the external potential  $\varphi_e(\mathbf{r})$ , the conductivity gradient  $\nabla\kappa_f(\mathbf{0})$ , the particle permittivity  $\epsilon_p$ , the particle conductivity  $\kappa_p$  (often zero), and the external flow field  $\mathbf{u}_e(\mathbf{r})$ .

### III. SINGLE SPHERE IN A UNIFORM FIELD

We first consider the dynamics of a single sphere in a uniform electric field  $\mathbf{E}_e = E_e\mathbf{e}_3$  and conductivity gradient  $\boldsymbol{\gamma} = \gamma\mathbf{e}_3$ , both directed in the 3-direction (normal to the electrode present in the experimental system [18]). We assume that the particle rotates in the 1-direction such that the system has mirror symmetry about the 23-plane. The condition of mirror symmetry further requires that the components  $p_1$ ,  $Q_{12}$ ,  $Q_{21}$ ,  $Q_{13}$ , and  $Q_{31}$  are zero. With these simplifications, the moment dynamics can be written as

$$\begin{aligned} \dot{q} &= -q - \frac{\gamma}{3}(2p_3 + E_e), \\ \dot{p}_2 &= -\Omega_1(p_3 - \epsilon'_{\text{cm}}E_e) - \frac{1}{\tau'}p_2 - \frac{3\gamma'}{5\tau'}Q_{23}, \\ \dot{p}_3 &= \Omega_1p_2 - \frac{1}{\tau'}(p_3 - \kappa'_{\text{cm}}E_e) - \frac{\gamma'}{\tau'}\left(q + \frac{3}{5}Q_{33}\right), \\ \dot{Q}_{22} &= -2\Omega_1Q_{23} - \frac{1}{\tau''}Q_{22} + \frac{2\gamma''}{3\tau''}(2p_3 + E_e), \\ \dot{Q}_{23} &= \Omega_1(Q_{22} - Q_{33}) - \frac{1}{\tau''}Q_{23} - \frac{2\gamma''}{\tau''}p_2, \\ \dot{Q}_{33} &= 2\Omega_1Q_{23} - \frac{1}{\tau''}Q_{33} - \frac{4\gamma''}{3\tau''}(2p_3 + E_e), \end{aligned} \quad (12)$$

where the angular velocity is  $\Omega_1 = \frac{1}{2}p_2E_e$ . Other nonzero components of the symmetric and traceless quadrupole moment are related to those above as  $Q_{32} = Q_{23}$  and  $Q_{11} = -Q_{22} - Q_{33}$ . The dimensionless parameters appearing in these equations depend on the particle permittivity  $\epsilon_p$  and conductivity  $\kappa_p$  as

$$\begin{aligned} \tau' &= \frac{\epsilon_p + 2}{\kappa_p + 2}, & \tau'' &= \frac{2\epsilon_p + 3}{2\kappa_p + 3}, \\ \gamma' &= \frac{\gamma}{\kappa_p + 2}, & \gamma'' &= \frac{\gamma}{2\kappa_p + 3}, \\ \epsilon'_{\text{cm}} &= \frac{\epsilon_p - 1}{\epsilon_p + 2}, & \epsilon''_{\text{cm}} &= \frac{\epsilon_p - 1}{2\epsilon_p + 3}, \\ \kappa'_{\text{cm}} &= \frac{\kappa_p - 1}{\kappa_p + 2}, & \kappa''_{\text{cm}} &= \frac{\kappa_p - 1}{2\kappa_p + 3}. \end{aligned} \quad (13)$$

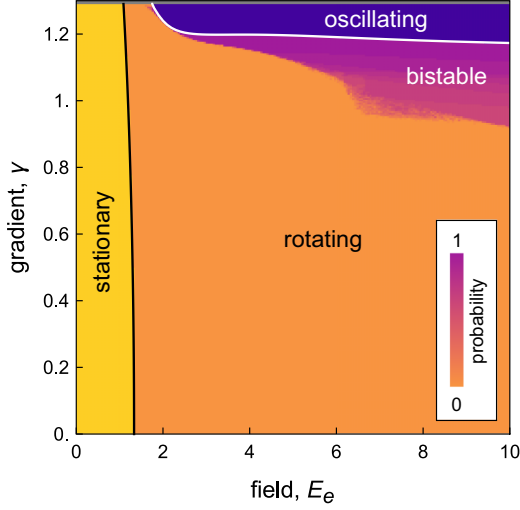


FIG. 2. Dynamical phase diagram showing the different behaviors of a single sphere in a uniform field as a function of the (dimensionless) field strength  $E_e$  and conductivity gradient  $\gamma$ . Other parameters are held constant:  $\varepsilon_p = 1.5$  and  $\kappa_p = 0$ . In the “stationary” region, there is a stable fixed point with  $\Omega_1 = 0$ . In the “rotating” region, there are two stable fixed points corresponding to steady particle rotation in either direction. In the “oscillating” region, there are no stable fixed points and the sphere rotates back and forth in a periodic or sometimes chaotic manner. In the “bistable” region, the stable limit cycle (or strange attractor) coexists with the stable fixed points for steady rotation. This region is identified by the probability of approaching the limit cycle for a specified distribution of initial conditions.

The problem is therefore specified by four dimensionless parameters: the particle permittivity  $\varepsilon_p$ , the particle conductivity  $\kappa_p$ , the external field  $E_e$ , and conductivity gradient  $\gamma$ . Figure 2 summarizes the different dynamical behaviors of the model as a function of the external field strength  $E_e$  and the conductivity gradient  $\gamma$  for a nonconductive particle  $\kappa_p = 0$  with permittivity  $\varepsilon_p = 1.5$ .

### A. Fixed points

For  $\gamma = 0$ , the fluid conductivity is spatially uniform, and the model dynamics (12) simplifies to the standard model for Quincke rotation. That model admits one fixed point in which the particle is stationary

$$\begin{aligned} p_3 &= \kappa'_{cm} E_e, \\ 0 &= q = p_2 = Q_{22} = Q_{23} = Q_{33}. \end{aligned} \quad (14)$$

Additionally, there are two fixed points in which the particle rotates with a constant velocity

$$\begin{aligned} \Omega_1 &= \pm \frac{1}{\tau'} \sqrt{(E_e/E_c)^2 - 1}, \\ p_2 &= \pm \frac{2}{E_e \tau'} \sqrt{(E_e/E_c)^2 - 1}, \\ p_3 &= \varepsilon'_{cm} E_e - \frac{2}{\tau' E_e}, \\ 0 &= q = Q_{22} = Q_{23} = Q_{33}, \end{aligned} \quad (15)$$

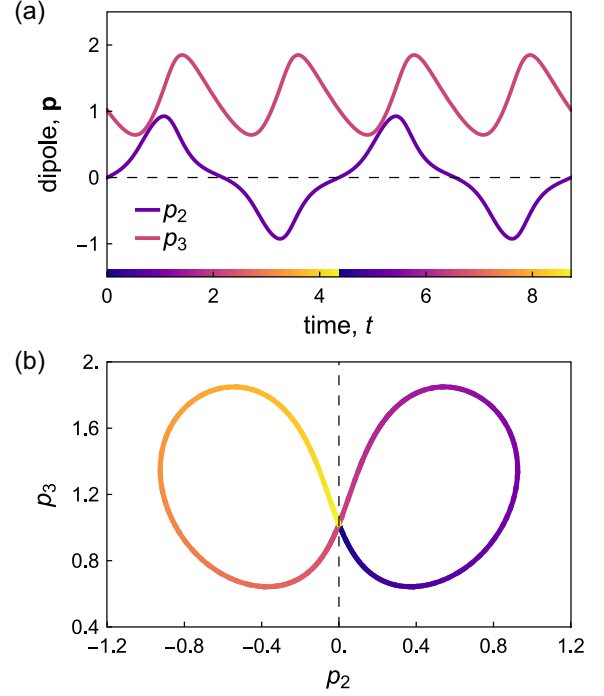


FIG. 3. (a) Oscillatory dynamics of the dipole  $\mathbf{p}$  for (dimensionless) parameters  $\varepsilon_p = 1.5$ ,  $\kappa_p = 0$ ,  $E_e = 10$ , and  $\gamma = 1.2$ . The oscillation period is  $T = 4.36$ . (b) Limit cycle projected onto the  $p_2$ - $p_3$  plane. The colormap shows the oscillation phase from (a).

where  $E_c = \sqrt{2/\tau'(\varepsilon'_{cm} - \kappa'_{cm})}$  is a critical field strength. The particle can rotate in either direction depending on the initial conditions. This rotating solution exists only when  $\varepsilon'_{cm} > \kappa'_{cm}$  or, equivalently, when  $\varepsilon_p/\kappa_p > 1$ . Moreover, linear stability analysis indicates that the rotating solution is stable only when the external field exceeds the critical field strength  $E_e > E_c$ ; for weaker fields, the particle does not rotate.

The addition of a finite conductivity gradient  $\gamma$  perturbs the stationary and rotating solutions; however, the qualitative behavior of the fixed points is unchanged. Below a critical field strength, the particle remains stationary (Fig. 2, “stationary” region). This stationary solution is stable for conductivity gradients below a critical value (here,  $\gamma = 1.291$  for  $\varepsilon_p = 1.5$ ); higher conductivity gradients lead to unphysical solutions and are not considered. At higher field strengths, there are two stable fixed points corresponding to particle rotation with a constant speed in either direction (Fig. 2, “rotating” region). Finally, at sufficiently high fields and conductivity gradients the rotating solution becomes unstable; there are no stable fixed points in this region of the phase diagram (Fig. 2, “oscillating” region). Instead, the particle rotates back and forth in an oscillatory or sometimes chaotic manner.

### B. Oscillatory solutions

Figure 3 shows the oscillatory dynamics of the dipole moment as predicted by Eq. (12) for  $E_c = 10$  and  $\gamma = 1.2$  [see also Fig. 1(b) for the angular velocity]. As detailed previously [18], Quincke oscillations derive from couplings

among the charge moments introduced by the conductivity gradient, which affects the charging rate at the particle surface. As described by the moment Eq. (12), the disturbance field produced by one moment leads to currents that alter the others. In particular, the quadrupolar disturbance contributes to the charging of the dipole moment as to reverse the direction of rotation, thereby enabling back-and-forth oscillations. Similar dynamics were observed in a related mechanical model of an overdamped water wheel [29] with a spatial gradient in the leakage rate [18]. The stable limit cycle is invariant to a symmetry operation that combines  $180^\circ$  rotation about the 3-axis and a  $T/2$  shift in the oscillation phase where  $T$  denotes the oscillation period. This phase-angle symmetry will be relevant to our description of the interactions between neighboring oscillators. The predicted oscillation frequency increases with increasing field strength in quantitative agreement with previous experimental observations (Fig. S2 [32]).

Within some parts of the “oscillating” region (Fig. 2), the particle exhibits asymmetric oscillations and chaotic dynamics (Figs. S3 and S4 [32]). Asymmetric limit cycles are characterized by a nonzero time average in the rotation velocity. Similar behaviors were observed in experiments on Quincke rollers, which sometimes roll across a surface with a time-periodic speed [18]. Chaotic dynamics are distinguished by aperiodic reversals the direction of particle rotation similar to that reported previously for Quincke rotation with finite particle inertia [30]. These behaviors are typically found at lower field strengths near the boundary between “rotating” and “oscillating” regions of the phase diagram (Fig. 2). In the present study, we focus our attention on the symmetric oscillations found at higher field strengths (Fig. 3).

Stable limit cycles and strange attractors are also found to coexist with the stable fixed points describing steady rotation (Fig. 3, “bistable” region). To map this bistable region of the phase diagram, we integrate the dynamics numerically from a distribution of initial conditions centered on a point on the attractor. Some of these initial conditions relax back to the attractor while others evolve to one of the two fixed points. The colormap in Fig. 3 shows the fraction of initial conditions that return to the limit cycle. Notably, the limit cycles and strange attractors in the bistable region sometimes lack the mirror symmetry implicit in Eq. (12). Instead, the direction of rotation in the 12-plane changes direction in a periodic or aperiodic manner (Fig. S5). To avoid this behavior, we focus our analysis on larger gradients  $\gamma$  in the “oscillating” region of the phase diagram (Fig. 3).

#### IV. TWO SPHERES IN A UNIFORM FIELD

We now consider the dynamics of two interacting spheres (denoted  $\alpha$  and  $\beta$ ) subject to a uniform field  $\mathbf{E}_e = E_e \mathbf{e}_3$  and conductivity gradient  $\nabla \kappa_f = \gamma \mathbf{e}_3$  in the 3-direction [Fig. 4(a)]. The spheres are separated by the displacement vector  $\mathbf{R} = \mathbf{r}_\beta - \mathbf{r}_\alpha$ , which is directed perpendicular to the applied field. Each sphere induces electric and hydrodynamic disturbance fields that influence the dynamics of the neighboring particle. The electric field at the center of sphere  $\alpha$  due both to the external field and to the disturbance field of sphere  $\beta$

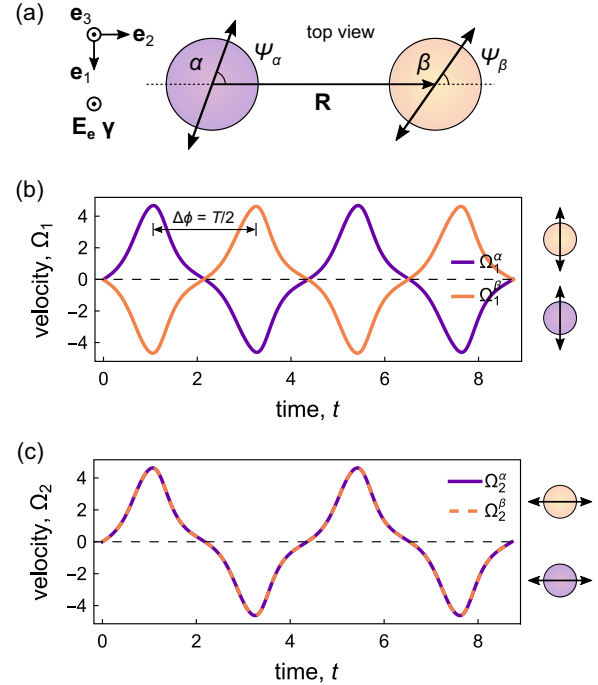


FIG. 4. (a) Schematic illustration of two oscillating spheres  $\alpha$  and  $\beta$  with angular orientations  $\psi_\alpha$  and  $\psi_\beta$  separated by a displacement  $\mathbf{R}$ . (b) With the constraint of mirror symmetry, the oscillators synchronize with a stable phase difference  $\Delta\phi = T/2$ . (c) Freely rotating spheres oscillate in phase ( $\Delta\phi = 0$ ) with orientations  $\psi_\alpha = \psi_\beta = \pi/2$ . The angular velocities are computed by numerical integration of the moment equations accounting for the far field interactions due to electric (16) and hydrodynamic (17) disturbances. The parameters are  $E_e = 10$ ,  $\gamma = 1.2$ ,  $\varepsilon_p = 1.5$ ,  $\kappa_p = 0$ , and  $R = 10$ .

is given by

$$-\nabla\varphi_e(\mathbf{r}_\alpha) = \mathbf{E}_e - \frac{q_\beta \hat{\mathbf{R}}}{R^2} + \frac{1}{R^3}(3\hat{\mathbf{R}}\hat{\mathbf{R}} - \delta) \cdot \mathbf{p}_\beta - \frac{1}{2R^4}(5\hat{\mathbf{R}}\hat{\mathbf{R}}\hat{\mathbf{R}} - 2\delta\hat{\mathbf{R}}) : \mathbf{Q}_\beta + \dots \quad (16)$$

When the spheres are widely separated (i.e.,  $R \gg 1$ ), only the leading-order terms are expected to contribute significantly. We substitute this expression for the field into Eqs. (5) to (7) for the dynamics of sphere  $\alpha$ , neglecting those terms of order  $R^{-4}$  and higher. The dynamics of sphere  $\beta$  is similarly perturbed by the disturbance field due to sphere  $\alpha$ .

The electric disturbance fields also contribute to the electric torques acting on each particle. We substitute Eq. (16) for the field at sphere  $\alpha$  into the torque balance (11), neglecting those terms of order  $R^{-4}$  and higher. The interactions we consider include charge-dipole interactions of order  $R^{-2}$ , dipole-dipole interactions of order  $R^{-3}$ , and charge-quadrupole interactions of order  $R^{-3}$ . In addition to electric interactions, we consider the leading-order hydrodynamic interactions between the two spheres. The fluid vorticity at the center of sphere  $\alpha$  due to rotation of sphere  $\beta$  is given by

$$\nabla \times \mathbf{u}_e(\mathbf{r}_\alpha) = -\frac{1}{R^3}(\delta - 3\hat{\mathbf{R}}\hat{\mathbf{R}})\Omega_\beta. \quad (17)$$

We substitute this expression into the torque balance (11) to account for far-field hydrodynamic interactions of order  $R^{-3}$ . We neglect the hydrodynamic force on sphere  $\alpha$  in the direction  $\mathbf{R} \times \boldsymbol{\Omega}_\beta$  and hold the positions of the two spheres constant. The torque on sphere  $\beta$  is similarly perturbed by the electric and hydrodynamic disturbance fields due to sphere  $\alpha$ .

With these electrostatic and hydrodynamic interactions, the coupled dynamics of the two spheres can be integrated numerically to identify their stable behavior(s). For spheres separated by a large distance ( $R = 10$ ) in the ‘‘oscillating’’ regime, we find one metastable attractor with mirror symmetry and one stable attractor without this symmetry [Figs. 4(b) and 4(c), respectively]. When mirror symmetry is imposed, the two in-line oscillators exhibit antiphase synchronization with a stable phase difference of  $T/2$  [Fig. 4(b)]. When this symmetry is relaxed, the particles evolve to a synchronized state characterized by in-phase oscillations aligned perpendicular to their line of centers [Fig. 4(c)].

## V. WEAKLY COUPLED PARTICLE OSCILLATORS

When the particles are sufficiently far apart, their coupled oscillatory dynamics can be accurately described using the formalism of weakly coupled oscillators [25,26]. In this approach, the dynamical state variable  $X(t)$  for each particle oscillator is replaced by a low-order approximation based on the phase  $\theta(t)$  and the angle  $\psi(t)$ . Here,  $X(t)$  is a 9-dimensional vector that describes the charge  $q(t)$ , the three components of dipole  $\mathbf{p}(t)$ , and the five independent components of the quadrupole  $\mathbf{Q}(t)$ . To derive evolution equations for the phase and angle, we write the dynamics of sphere  $\alpha$  as

$$\dot{X}_\alpha = F(X_\alpha) + R^{-2}I_2(X_\alpha, X_\beta) + R^{-3}I_3(X_\alpha, X_\beta) + \dots, \quad (18)$$

where  $F(X_\alpha)$  describes the dynamics of the individual sphere, and the functions  $I_n(X_\alpha, X_\beta)$  describe interactions with a neighboring sphere  $\beta$ . The inverse distance  $R^{-1}$  plays the role of the small parameter in a singular perturbation analysis.

For a single particle, the dynamics on the limit cycle  $X_{\text{LC}}(t)$  can be parameterized by the phase  $\theta$  and the angle  $\psi$  of the oscillator. The oscillation phase is defined as

$$\theta(t) = (t + \phi) \pmod{T}, \quad (19)$$

where  $T$  is the oscillation period and  $\phi$  is the relative phase. We define the relative phase such that  $\theta = 0$  corresponds to zero angular velocity prior to rotation in the positive one-direction [see Fig. 1(a)]. Similarly, we choose the angle  $\psi = 0$  to describe oscillatory rotations about the 1-axis. Other limit cycles are obtained by rotation of the dipole and quadrupole in the three-direction by an angle  $\psi$ . Away from the limit cycle, we map each point  $X(t)$  in the basin of the limit cycle to the asymptotic phase  $\Phi[X(t)]$  and angle  $\Psi[X(t)]$  to which it evolves—that is,  $\Phi[X(t)] = \theta(t)$  and  $\Psi[X(t)] = \psi(t)$  as  $t \rightarrow \infty$ .

The phase of oscillator  $\alpha$  evolves in time as

$$\begin{aligned} \dot{\theta}_\alpha &= \nabla_X \Phi(X_\alpha) \cdot \dot{X}_\alpha \\ &= 1 + R^{-2} \nabla_X \Phi(X_\alpha) \cdot I_2(X_\alpha, X_\beta) + \dots, \end{aligned} \quad (20)$$

where we made use of Eq. (18) and the fact that  $\nabla_X \Phi(X_\alpha) \cdot F(X_\alpha) = 1$ . For weakly coupled oscillators, the state variable

$X_\alpha(t)$  is well approximated by its value on the limit cycle  $X_\alpha(t) \approx X_{\text{LC}}(t + \phi_\alpha, \psi_\alpha)$  as parameterized by the relative phase  $\phi_\alpha$  and the angle  $\psi_\alpha$ . Substituting this approximation into Eq. (20) and averaging the dynamics over one oscillation cycle, we obtain the following approximate dynamics for the relative phase of oscillator  $\alpha$ :

$$\begin{aligned} \dot{\phi}_\alpha &= \frac{1}{R^2 T} \int_0^T \nabla_X \Phi[X_{\text{LC}}(t + \phi_\alpha, \psi_\alpha)] \\ &\quad \cdot I_2[X_{\text{LC}}(t + \phi_\alpha, \psi_\alpha), X_{\text{LC}}(t + \phi_\beta, \psi_\beta)] dt + \dots \\ &= R^{-2} H_2^\phi(\psi_\alpha, \psi_\beta, \Delta\phi) + R^{-3} H_3^\phi(\psi_\alpha, \psi_\beta, \Delta\phi) + \dots, \end{aligned} \quad (21)$$

where  $H_2^\phi(\psi_\alpha, \psi_\beta, \Delta\phi)$  and  $H_3^\phi(\psi_\alpha, \psi_\beta, \Delta\phi)$  are oscillation-averaged interaction functions that depend on the oscillator angles  $\psi_\alpha$  and  $\psi_\beta$  and the phase difference  $\Delta\phi = \phi_\beta - \phi_\alpha$ . We use the adjoint method [26,31] to compute the phase response curve (PRC)  $\nabla_X \Phi[X_{\text{LC}}(\theta, \psi)]$ , which describes the shift in phase induced by an infinitesimal perturbation of the limit cycle. The interaction functions  $I_2(X_\alpha, X_\beta)$  and  $I_3(X_\alpha, X_\beta)$  for in-line oscillators are summarized in the Appendix.

We derive the oscillation-averaged evolution of the angle  $\psi_\alpha$  in an analogous fashion as

$$\begin{aligned} \dot{\psi}_\alpha &= \frac{1}{R^2 T} \int_0^T \nabla_X \Psi[X_{\text{LC}}(t + \phi_\alpha, \psi_\alpha)] \\ &\quad \cdot I_2[X_{\text{LC}}(t + \phi_\alpha, \psi_\alpha), X_{\text{LC}}(t + \phi_\beta, \psi_\beta)] dt + \dots \\ &= R^{-2} H_2^\psi(\psi_\alpha, \psi_\beta, \Delta\phi) + R^{-3} H_3^\psi(\psi_\alpha, \psi_\beta, \Delta\phi) + \dots, \end{aligned} \quad (22)$$

where  $H_2^\psi(\psi_\alpha, \psi_\beta, \Delta\phi)$  and  $H_3^\psi(\psi_\alpha, \psi_\beta, \Delta\phi)$  are interaction functions for the oscillator angle. Here, the angle response curve  $\nabla_X \Psi[X_{\text{LC}}(\theta, \psi)]$  describes how perturbations to the limit cycle alter the oscillator angle. By definition, changes in the oscillator angle due to rotation in the 3-direction (parallel to the external field and the conductivity gradient) do not alter its phase. As a result, the angle response vector  $\nabla_X \Psi$ , which points in the direction of increasing angle, must be normal to phase response vector  $\nabla_X \Phi$ , which points in the direction of increasing phase.

To evaluate the angle response curve  $\nabla_X \Psi[X_{\text{LC}}(\theta, \psi)]$ , we introduce a transformation function  $R_3(\psi, X)$  that rotates the components of the state vector  $X$  about the 3-axis by the angle  $\psi$ . Using this function, the limit cycle for angle  $\psi$  is related to that for zero angle as  $X_{\text{LC}}(\theta, \psi) = R_3[\psi, X_{\text{LC}}(\theta, 0)]$ . Differentiating the limit cycle  $X_{\text{LC}}(\theta, \psi)$  with respect to  $\psi$ , we obtain a vector  $\partial_\psi R_3[\psi, X_{\text{LC}}(\theta, 0)]$  that points normal to the phase response vector in the direction of increasing angle. Due to the rotational symmetry of the dynamics about the 3-axis, the angle response curve  $\nabla_X \Psi[X_{\text{LC}}(\theta, \psi)]$  must be parallel to this vector such that

$$\nabla_X \Psi(X_{\text{LC}}(\theta, \psi)) = \frac{\partial_\psi R_3[\psi, X_{\text{LC}}(\theta, 0)]}{|\partial_\psi R_3[\psi, X_{\text{LC}}(\theta, 0)]|^2}. \quad (23)$$

Here, the normalization condition  $\nabla_X \Psi[X_{\text{LC}}(\theta, \psi)] \cdot \partial_\psi R_3[\psi, X_{\text{LC}}(\theta, 0)] = 1$  is obtained by differentiating the angle map  $\Psi[X_{\text{LC}}(\theta, \psi)] = \psi$  with respect to  $\psi$ .

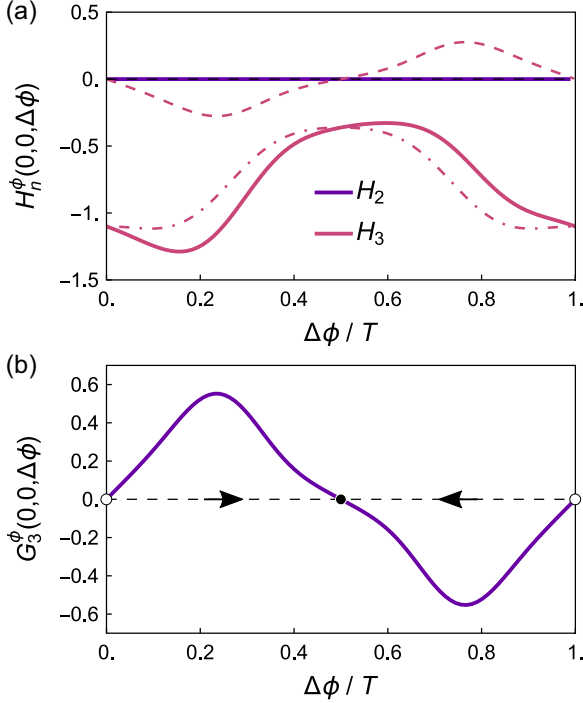


FIG. 5. Phase interaction functions for two weakly coupled, in-line oscillators as a function of their phase difference  $\Delta\phi = \phi_\beta - \phi_\alpha$ . (a) Oscillation-averaged interaction functions  $H_2^\phi(\psi_\alpha, \psi_\beta, \Delta\phi)$  and  $H_3^\phi(\psi_\alpha, \psi_\beta, \Delta\phi)$  of Eq. (21) computed numerically for parameters  $E_e = 10$ ,  $\gamma = 1.2$ ,  $\varepsilon_p = 1.5$ , and  $\kappa_p = 0$  with in-line orientation  $\psi_\alpha = \psi_\beta = 0$ . Dashed and dot-dashed curves denote the odd and even parts of  $H_3$ , respectively. (b) The  $G_3(\psi_\alpha, \psi_\beta, \Delta\phi)$  function of Eq. (24) describes the evolution of the phase difference  $\Delta\phi$  for  $\psi_\alpha = \psi_\beta = 0$ . The filled and open circles denote the stable and unstable fixed points of the phase difference.

#### A. Two in-line oscillators: $\psi_\alpha = \psi_\beta = 0$

We first consider the case of two particles  $\alpha$  and  $\beta$  oscillating in a common direction perpendicular to both the external field  $E_e \mathbf{e}_3$  and the displacement vector  $R \mathbf{e}_2$  [Fig. 4(a) with  $\psi_\alpha = \psi_\beta = 0$ ]. For each oscillator, the angle is fixed to zero; however, the relative phase is free to evolve due to electrostatic and hydrodynamic interactions. Figure 5(a) shows the interaction functions  $H_2^\psi(0, 0, \Delta\phi)$  and  $H_3^\psi(0, 0, \Delta\phi)$  as a function of the phase difference  $\Delta\phi = \phi_\beta - \phi_\alpha$  for in-line oscillators with  $\psi_\alpha = \psi_\beta = 0$ . Notably, the second-order interaction function is zero to within the precision of the computation. The disturbance fields induced by the charges  $q_\alpha$  and  $q_\beta$  do not alter the oscillator phases. For this configuration, the leading-order contribution is the third-order interaction proportional to  $R^{-3}$ .

The evolution of the phase difference  $\Delta\phi = \phi_\beta - \phi_\alpha$  is determined by the odd part of the interaction function

$$\begin{aligned} \dot{\Delta\phi} &= R^{-3} [H_3^\phi(0, 0, -\Delta\phi) - H_3^\phi(0, 0, \Delta\phi)] \\ &= R^{-3} G_3^\phi(0, 0, \Delta\phi). \end{aligned} \quad (24)$$

The roots of the  $G_3^\phi(0, 0, \Delta\phi)$  function correspond to synchronized states characterized by a constant phase difference

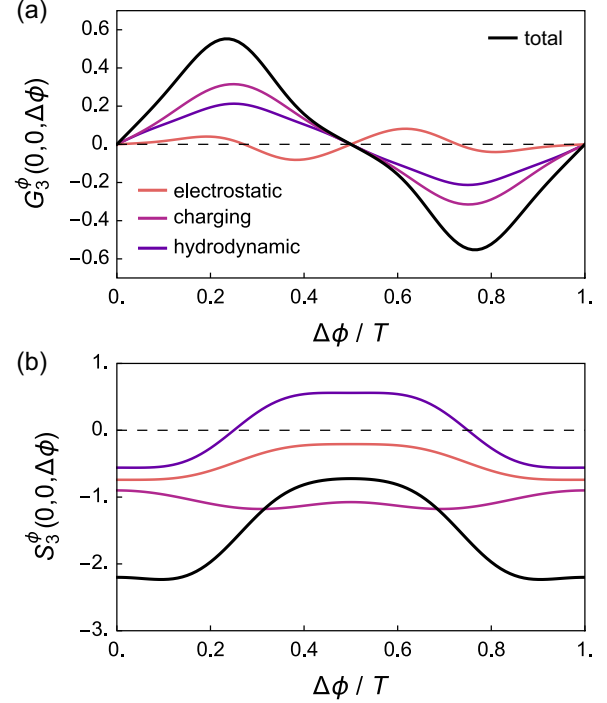


FIG. 6. Decomposition of the interaction functions for two inline oscillators ( $\psi_\alpha = \psi_\beta = 0$ ) into electrostatic, charging, and hydrodynamic contributions. (a)  $G_3^\phi(\psi_\alpha, \psi_\beta, \Delta\phi)$  function of Eq. (24) describing the evolution of the phase difference. (b)  $S_3^\phi(\psi_\alpha, \psi_\beta, \Delta\phi)$  of Eq. (25) describing the evolution of the phase sum. The functions are calculated numerically for parameters  $E_e = 10$ ,  $\gamma = 1.2$ ,  $\varepsilon_p = 1.5$ , and  $\kappa_p = 0$ .

[Fig. 5(b)]. For the parameter values investigated, two in-line oscillators synchronize with a stable phase difference of  $\Delta\phi = T/2$  in agreement with numerical simulations presented above [cf. Figs. 5(b) and 4(b)].

The interactions between the two oscillators can also alter the frequency of their oscillations as described by the even part of the interaction function [Fig. 5(a), dot-dashed curve]. The phase sum  $\Sigma\phi = \phi_\alpha + \phi_\beta$  evolves as

$$\begin{aligned} \dot{\Sigma\phi} &= R^{-3} [H_3^\phi(0, 0, \Delta\phi) + H_3^\phi(0, 0, -\Delta\phi)] \\ &= R^{-3} S_3^\phi(0, 0, \Delta\phi). \end{aligned} \quad (25)$$

Here, the  $S_3^\phi(0, 0, \Delta\phi)$  function is negative for all phase differences, which implies that interactions act to slow the frequency of oscillations.

To better understand the physical origins of these interactions, we decompose the leading-order interaction functions  $G_3^\phi(0, 0, \Delta\phi)$  and  $S_3^\phi(0, 0, \Delta\phi)$  into three contributions: electric *charging* interactions that alter the moment dynamics of Eqs. (5) to (7), *electrostatic* interactions that alter the electric torque in Eq. (11), and *hydrodynamic* interactions that alter the hydrodynamic torque in Eq. (11). As illustrated in Fig. 6, each of these three interactions make significant contributions to the synchronization and frequency of coupled Quincke oscillators. Hydrodynamic interactions favor antiphase synchronization for which the hydrodynamic resistance of particle rotation is minimal [Fig. 6(a), hydro-

dynamic]. Under these conditions, the  $S_3^\phi(0, 0, \Delta\phi)$  function is positive indicating an increase in the frequency for the coupled oscillators [Fig. 6(b), hydrodynamic]. Such antiphase synchronization is not favored by the electrostatic interactions due to dipole-dipole repulsion [Fig. 6(a), electrostatic]; however, these effects are insufficient to determine the overall response. The dipolar field of each particle acts to oppose the external field at the site of its neighbor thereby slowing its oscillation frequency [Fig. 6(b), charging]. These electric charging interactions also favor antiphase synchronization [Fig. 6(a), charging]; however, the physical mechanisms of this effect are not intuitive.

### B. Two free oscillators

Relaxing the in-line constraint that  $\psi_\alpha = \psi_\beta = 0$ , the behavior of two weakly coupled Quincke oscillators is governed by the three-dimensional (3D) dynamical system

$$\begin{aligned}\dot{\psi}_\alpha &= R^{-3} H_3^\psi(\psi_\alpha, \psi_\beta, \Delta\phi), \\ \dot{\psi}_\beta &= R^{-3} H_3^\psi(\psi_\beta, \psi_\alpha, -\Delta\phi), \\ \dot{\Delta\phi} &= R^{-3} G_3^\phi(\psi_\alpha, \psi_\beta, \Delta\phi),\end{aligned}\quad (26)$$

which describes the evolution of the oscillator angles  $\psi_\alpha$  and  $\psi_\beta$  and the phase difference  $\Delta\phi = \phi_\beta - \phi_\alpha$ . For brevity, we denote these dynamics as  $\dot{\mathbf{X}} = \mathbf{F}(\mathbf{X})$  where each component of  $\mathbf{F}(\mathbf{X})$  is a  $2\pi$ -periodic function its vector argument  $\mathbf{X} = [\psi_\alpha, \psi_\beta, \omega\Delta\phi]^\top$  where  $\omega = 2\pi/T$  is the natural frequency of the oscillator. Figure 7 shows the 3D phase portrait for this system highlighting its various symmetries and fixed points.

The dynamics of Eq. (26) is characterized by several symmetries that significantly constrain the behavior of the system: phase-angle, permutation, and mirror symmetries. As discussed above, phase-angle symmetry implies that a shift in the phase of either oscillator by  $T/2$  is equivalent to a change in angle by  $\pi$ . Together with the periodicity condition, this symmetry implies that

$$\mathbf{F}(\mathbf{X}) = \mathbf{F}(\mathbf{X} + n_1\mathbf{a}_1 + n_2\mathbf{a}_2 + n_3\mathbf{a}_3), \quad (27)$$

where  $\mathbf{a}_1 = [\pi, \pi, 0]^\top$ ,  $\mathbf{a}_2 = [\pi, 0, \pi]^\top$ , and  $\mathbf{a}_3 = [0, \pi, \pi]^\top$  are primitive basis vectors and  $n_1, n_2$ , and  $n_3$  are arbitrary integers. This translational symmetry is identical to that of a face centered cubic (FCC) lattice in crystallography; the Wigner-Seitz cell is the rhombic dodecahedron illustrated in Fig. 7(a). This primitive unit cell can be used to fill phase space using translations along the basis vectors.

Additionally, invariance of the dynamics under permutation of the indices  $\alpha$  and  $\beta$  implies that

$$\mathbf{F}(\mathbf{X}) = Q\mathbf{F}(Q\mathbf{X}) \quad \text{with} \quad Q = \begin{bmatrix} 0 & 1 & 0 \\ 1 & 0 & 0 \\ 0 & 0 & -1 \end{bmatrix}. \quad (28)$$

This symmetry operation can be interpreted as a  $180^\circ$  rotation in phase space about the basis vector  $\mathbf{a}_1$ . Finally, because the motion of each oscillator is achiral, their coupled dynamics

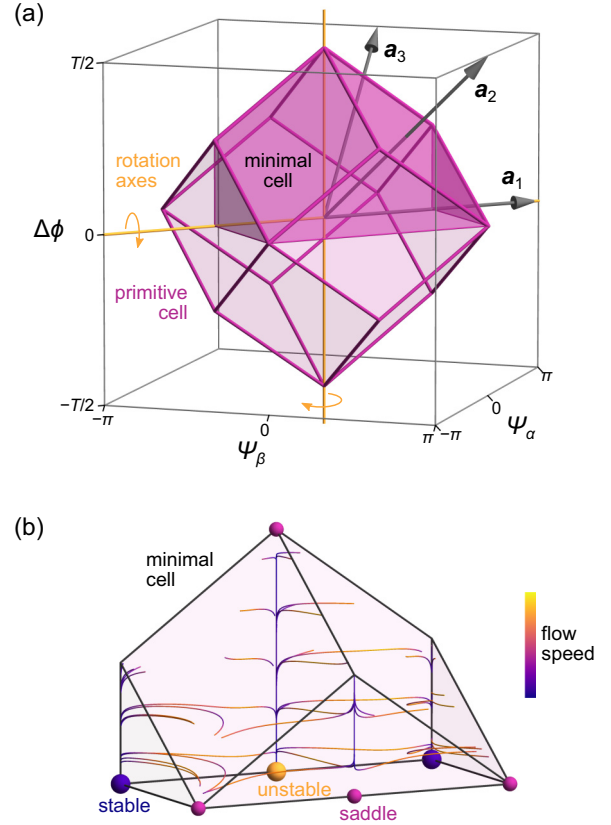


FIG. 7. Three-dimensional phase portrait of the dynamics for two weakly coupled Quincke oscillators. (a) The periodic domain of the variables  $\psi_\alpha, \psi_\beta, \Delta\phi$  can be divided using symmetries of the dynamics, namely, translation along the basis vectors  $\mathbf{a}_1, \mathbf{a}_2, \mathbf{a}_3$  and rotation about the yellow axes. Knowledge of the dynamics within the minimal cell is sufficient to reconstruct the full system. (b) Within the minimal cell, streamlines of the dynamics flow from the unstable fixed points (yellow) to the stable fixed points (blue). Streamlines are computed numerically for parameters  $E_e = 10$ ,  $\gamma = 1.2$ ,  $\varepsilon_p = 1.5$ , and  $\kappa_p = 0$ .

exhibits the following symmetry with respect to mirror reflection about the  $\mathbf{e}_1$  direction [Fig. 4(a)]:

$$\mathbf{F}(\mathbf{X}) = Q\mathbf{F}(Q\mathbf{X}) \quad \text{with} \quad Q = \begin{bmatrix} -1 & 0 & 0 \\ 0 & -1 & 0 \\ 0 & 0 & 1 \end{bmatrix}. \quad (29)$$

This operation can be interpreted as a  $180^\circ$  rotation in phase space about the vector  $[0, 0, 1]^\top$ . These two-fold rotational symmetries in phase space are illustrated by the yellow axes in Fig. 7(a). Using these symmetries, we identify a minimal cell in phase space which concisely summarizes the system's dynamics [Fig. 7(b)].

Linear stability analysis of Eq. (26) reveals one stable fixed point located at  $\psi_\alpha = \psi_\beta = \pi/2$ ,  $\Delta\phi = 0$  [Fig. 4(b), blue spheres]. This point corresponds to synchronized rotation along the axis connecting the two oscillators in agreement with the numerical results above [Fig. 4(c)]. Inspection of the eigenmodes shows how the system relaxes to this stable solution. The angle sum  $\psi_\alpha + \psi_\beta$  and the angle difference  $\psi_\alpha - \psi_\beta$  evolve rapidly to their asymptotic values in



pursuit of parallel alignment. Once aligned, the respective phases of the two oscillators slowly relax into synchrony (Fig. S6 [32]). The unstable fixed points and saddle points of the dynamics are also illustrated in the minimal cell of Fig. 4(b).

Using the above symmetries, we can create accurate parametric approximations of the interaction functions of the form

$$H_3^\psi(\psi_\alpha, \psi_\beta, \Delta\phi) = \sum_{jkl} A_{jkl}^\phi e^{ij(\psi_\alpha + \psi_\beta - \Delta\phi) + k(\psi_\alpha - \psi_\beta + \Delta\phi) + l(-\psi_\alpha + \psi_\beta + \Delta\phi)}, \quad (30)$$

where  $j, k, l = 0, \pm 1, \pm 2, \dots$ , are integers, and  $A_{jkl}^\phi$  are complex coefficients. This Fourier series preserves the translational symmetry of Eq. (27). Additionally, the mirror symmetry condition of Eq. (29) provides additional relationships among the coefficients. Accounting for these symmetries, the first few terms of the angle interaction function are given by

$$\begin{aligned} H_3^\psi(\psi_\alpha, \psi_\beta, \Delta\phi) &= B_1^\psi \sin 2\psi_\alpha + B_2^\psi \sin 2\psi_\beta \\ &+ (C_1^\psi \sin \Delta\phi + C_2^\psi \cos \Delta\phi) \sin(\psi_\beta - \psi_\alpha) \\ &+ (C_3^\psi \sin \Delta\phi + C_4^\psi \cos \Delta\phi) \sin(\psi_\beta + \psi_\alpha) \\ &+ D_1^\psi \sin(2\psi_\beta - 2\psi_\alpha) + D_2^\psi \sin(2\psi_\beta + 2\psi_\alpha) \\ &+ (E_1^\psi \sin 3\Delta\phi + E_2^\psi \cos 3\Delta\phi) \sin(\psi_\beta - \psi_\alpha) \\ &+ (E_3^\psi \sin 3\Delta\phi + E_4^\psi \cos 3\Delta\phi) \sin(\psi_\beta + \psi_\alpha) + \dots, \end{aligned} \quad (31)$$

where the  $A^\psi, B^\psi, C^\psi, \dots$ , are coefficients to be determined. Similarly, the phase interaction function can be approximated as

$$\begin{aligned} H_3^\phi(\psi_\alpha, \psi_\beta, \Delta\phi) &= A^\phi + B_1^\phi \cos 2\psi_\alpha + B_2^\phi \cos 2\psi_\beta + B_3^\phi \sin 2\Delta\phi \\ &+ B_4^\phi \cos 2\Delta\phi \\ &+ (C_1^\phi \sin \Delta\phi + C_2^\phi \cos \Delta\phi) \cos(\psi_\beta - \psi_\alpha) \\ &+ (C_3^\phi \sin \Delta\phi + C_4^\phi \cos \Delta\phi) \cos(\psi_\beta + \psi_\alpha) \\ &+ D_1^\phi \cos(2\psi_\beta - 2\psi_\alpha) + D_2^\phi \cos(2\psi_\beta + 2\psi_\alpha) \\ &+ (E_1^\phi \sin 3\Delta\phi + E_2^\phi \cos 3\Delta\phi) \cos(\psi_\beta - \psi_\alpha) \\ &+ (E_3^\phi \sin 3\Delta\phi + E_4^\phi \cos 3\Delta\phi) \cos(\psi_\beta + \psi_\alpha) + \dots \end{aligned} \quad (32)$$

To estimate the coefficients, we first compute the interaction functions on a regular grid of  $34 \times 34 \times 34$  points in  $\psi_\alpha, \psi_\beta, \Delta\phi$  phase space. The coefficients are estimated from these data using linear regression. This parametric approximation agrees with the numerically computed interaction function to within 5%. Table I summarizes the coefficients using the specific parameter values considered throughout. Notably, these dynamics cannot be described by a gradient system, that is,  $\mathbf{F}(\mathbf{X}) \neq \nabla U(\mathbf{X})$  for some scalar potential

TABLE I. Coefficients for the approximate interaction functions  $H_3^\psi(\psi_\alpha, \psi_\beta, \Delta\phi)$  and  $H_3^\phi(\psi_\alpha, \psi_\beta, \Delta\phi)$  of Eqs. (31) and (32) obtained by linear regression for parameters  $E_c = 10$ ,  $\gamma = 1.2$ ,  $\varepsilon_p = 1.5$ , and  $\kappa_p = 0$ .

$n$	1	2	3	4
$B_n^\psi$	5.9863	-0.0003	-	-
$C_n^\psi$	-0.2423	0.1550	-1.2558	0.3454
$D_n^\psi$	0.0003	0.0001	-	-
$E_n^\psi$	0.0690	0.02174	0.2845	-0.0237
$A_n^\phi$	-0.4548	-	-	-
$B_n^\phi$	-0.3210	0.0000	-0.0224	0.0443
$C_n^\phi$	0.0151	0.1349	-0.2492	-0.5552
$D_n^\phi$	0.0000	0.0000	-	-
$E_n^\phi$	0.0044	-0.0180	0.0309	0.0704

$U(\mathbf{X})$ . As a result, other behaviors such as stable limit cycles or strange attractors may be possible for coupled Quincke oscillators under different conditions.

In our present analysis, the positions of the two oscillators are held constant while their oscillation angles and phases evolve to a synchronized state of parallel alignment. Relaxing this constraint, electrostatic interactions between the like charged particles act to increase the interparticle separation  $R$  at a rate proportional to  $R^{-2}$ . Hydrodynamic interactions due to particle rotation leads to particle motion perpendicular to the line of centers at a rate proportional to  $R^{-2}$ ; however, such oscillatory motions are expected to average to zero in the far field. Future efforts to describe the coupled dynamics of Quincke oscillators should consider the effects of the electrode surface, which is expected to alter the qualitative behavior of the interaction functions.

## VI. CONCLUSION

The dynamical model developed herein can be used to describe the collective behaviors of many Quincke oscillators interacting via electric and hydrodynamic interactions. In the limit of weak coupling, these mobile oscillators are characterized by their position, angle, and phase, which evolve in time due to pairwise, nonreciprocal interactions with neighboring particles. Here, we show that two such particles prefer to synchronize, align, and accelerate their rotary oscillations along the line of centers. For three or more particles in the plane normal to the field, competition among these mutually incompatible tendencies is expected to produce a variety of dynamical behaviors that depend on the particle configuration. To enable comparison with experimental studies, future work should consider the effects of the electrode surface in mediating the electric and hydrodynamic interactions among the particles. In particular, particle motions due to rotation-translation coupling at the solid surface may enable new types of time-averaged interactions that direct the formation of dynamic particle assemblies. These and other colloidal oscillators can provide useful models of active matter based on self-oscillating units with which to understand and engineer swarmalator dynamics.

**APPENDIX: INTERACTION FUNCTION FOR IN-LINE OSCILLATORS**

We consider two in-line oscillators ( $\psi_\alpha = \psi_\beta = 0$ ) separated by the displacement  $\mathbf{R} = R\mathbf{e}_2$  and subject the external field  $\mathbf{E}_e = E_e\mathbf{e}_3$  and the conductivity gradient  $\nabla\kappa_f = \gamma\mathbf{e}_3$ . We assume the system has mirror symmetry about the 23-plane, which implies that several components of the dipole and quadrupole moments are zero (namely,  $p_1 = Q_{12} = Q_{21} = Q_{13} = Q_{31} = 0$  for each oscillator  $\alpha$  and  $\beta$ ). The second-order interaction function  $I_2(X_\alpha, X_\beta)$  appearing in Eq. (18) has the following nonzero components:

$$\begin{aligned} I_2^{p_2}(X_\alpha, X_\beta) &= -\Omega_1^{\alpha 2}(p_3^\alpha - \varepsilon'_{\text{cm}}E_e) - \frac{\kappa'_{\text{cm}}}{\tau'}q^\beta, \\ I_2^{p_3}(X_\alpha, X_\beta) &= \Omega_1^{\alpha 2}p_2^\alpha + \frac{1}{2}p_2^\alpha E_e \varepsilon'_{\text{cm}}q^\beta, \\ I_2^{Q_{22}}(X_\alpha, X_\beta) &= -I_2^{Q_{33}}(X_\alpha, X_\beta) = -2\Omega_1^{\alpha 2}Q_{23}^\alpha, \\ I_2^{Q_{23}}(X_\alpha, X_\beta) &= \Omega_1^{\alpha 2}(Q_{22}^\alpha - Q_{33}^\alpha) + \frac{\gamma_3''}{\tau''}q^\beta, \\ \text{with } \Omega_1^{\alpha 2} &= \frac{1}{2}p_3^\alpha q^\beta. \end{aligned} \tag{A1}$$

Similarly, the third-order interaction function is

$$\begin{aligned} I_3^q(X_\alpha, X_\beta) &= \frac{\gamma}{3\tau}p_3^\beta, \\ I_3^{p_2}(X_\alpha, X_\beta) &= -\Omega_1^{\alpha 3}(p_3^\alpha - \varepsilon'_{\text{cm}}E_e) - \frac{1}{2}p_2^\alpha E_e \varepsilon'_{\text{cm}}p_3^\beta \\ &\quad + \frac{2\kappa'_{\text{cm}}}{\tau'}p_2^\beta, \\ I_3^{p_3}(X_\alpha, X_\beta) &= \Omega_1^{\alpha 3}p_2^\alpha - p_2^\alpha E_e \varepsilon'_{\text{cm}}p_2^\beta - \frac{\kappa'_{\text{cm}}}{\tau'}p_3^\beta - \frac{2\gamma'}{5\tau'}q^\beta, \\ I_3^{Q_{22}}(X_\alpha, X_\beta) &= -2\Omega_1^{\alpha 3}Q_{23}^\alpha - \frac{4\kappa''_{\text{cm}}}{\tau''}q^\beta - \frac{2\gamma''}{3\tau''}p_3^\beta, \\ I_3^{Q_{23}}(X_\alpha, X_\beta) &= \Omega_1^{\alpha 3}(Q_{22}^\alpha - Q_{33}^\alpha) + 3p_2^\alpha E_e \varepsilon''_{\text{cm}}q^\beta - \frac{2\gamma''}{\tau''}p_2^\beta, \\ I_3^{Q_{33}}(X_\alpha, X_\beta) &= 2\Omega_1^{\alpha 3}Q_{23}^\alpha + \frac{2\kappa''_{\text{cm}}}{\tau''}q^\beta + \frac{4\gamma''}{3\tau''}p_3^\beta, \\ \text{with } \Omega_1^{\alpha 3} &= \frac{1}{2}\left(Q_{23}^\alpha q^\beta - p_2^\alpha p_3^\beta - 2p_3^\alpha p_2^\beta - \frac{1}{2}p_2^\beta E_e\right). \end{aligned} \tag{A2}$$

---

[1] K. P. O’Keeffe, H. Hong, and S. H. Strogatz, Oscillators that sync and swarm, *Nat. Commun.* **8**, 1504 (2017).

[2] M. Fruchart, R. Hanai, P. B. Littlewood, and V. Vitelli, Non-reciprocal phase transitions, *Nature (London)* **592**, 363 (2021).

[3] J. O’Byrne, Y. Kafri, J. Tailleur, and F. van Wijland, Time irreversibility in active matter, from micro to macro, *Nat. Rev. Phys.* **4**, 167 (2022).

[4] C. Bechinger, R. Di Leonardo, H. Löwen, C. Reichhardt, G. Volpe, and G. Volpe, Active particles in complex and crowded environments, *Rev. Mod. Phys.* **88**, 045006 (2016).

[5] J. R. Howse, R. A. L. Jones, A. J. Ryan, T. Gough, R. Vafabakhsh, and R. Golestanian, Self-Motile Colloidal Particles: From Directed Propulsion to Random Walk, *Phys. Rev. Lett.* **99**, 048102 (2007).

[6] A. M. Brooks, M. Tasinkevych, S. Sabrina, D. Velegol, A. Sen, and K. J. M. Bishop, Shape-directed rotation of homogeneous micromotors via catalytic self-electrophoresis, *Nat. Commun.* **10**, 495 (2019).

[7] S. Gangwal, O. J. Cayre, M. Z. Bazant, and O. D. Velev, Induced-Charge Electrophoresis of Metallo-dielectric Particles, *Phys. Rev. Lett.* **100**, 058302 (2008).

[8] S. Sabrina, M. Tasinkevych, S. Ahmed, A. M. Brooks, M. Olvera de la Cruz, T. E. Mallouk, and K. J. M. Bishop, Shape-directed microspinnners powered by ultrasound, *ACS Nano* **12**, 2939 (2018).

[9] K. J. M. Bishop, S. L. Biswal, and B. Bharti, Active colloids as models, materials, and machines, *Annu. Rev. Chem. Biomol. Eng.* **14**, (2023).

[10] J. Yan, M. Bloom, S. C. Bae, E. Luijten, and S. Granick, Linking synchronization to self-assembly using magnetic janus colloids, *Nature (London)* **491**, 578 (2012).

[11] Y. Dou, S. Pandey, C. A. Cartier, O. Miller, and K. J. M. Bishop, Emergence of traveling waves in linear arrays of electromechanical oscillators, *Commun. Phys.* **1**, 85 (2018).

[12] Y. Dou, C. A. Cartier, W. Fei, S. Pandey, S. Razavi, I. Kretzschmar, and K. J. Bishop, Directed motion of metallo-dielectric particles by contact charge electrophoresis, *Langmuir* **32**, 13167 (2016).

[13] B. Zhang, A. Sokolov, and A. Snezhko, Reconfigurable emergent patterns in active chiral fluids, *Nat. Commun.* **11**, 4401 (2020).

[14] M. P. N. Juniper, A. V. Straube, R. Besseling, D. G. A. L. Aarts, and R. Dullens, Microscopic dynamics of synchronization in driven colloids, *Nat. Commun.* **6**, 7187 (2015).

[15] J. Kotar, M. Leoni, B. Bassetti, M. C. Lagomarsino, and P. Cicuti, Hydrodynamic synchronization of colloidal oscillators, *Proc. Natl. Acad. Sci. USA* **107**, 7669 (2010).

[16] J. Kotar, L. Debono, N. Bruot, S. Box, D. Phillips, S. Simpson, S. Hanna, and P. Cicuti, Optimal Hydrodynamic Synchronization of Colloidal Rotors, *Phys. Rev. Lett.* **111**, 228103 (2013).

[17] G. Quincke, Ueber rotationen im constanten electrischen felde, *Ann. Phys. Chem.* **295**, 417 (1896).

[18] Z. Zhang, H. Yuan, Y. Dou, M. O. de la Cruz, and K. J. M. Bishop, Quincke Oscillations of Colloids at Planar Electrodes, *Phys. Rev. Lett.* **126**, 258001 (2021).

[19] A. Bricard, J.-B. Caussin, N. Desreumaux, O. Dauchot, and D. Bartolo, Emergence of macroscopic directed motion in populations of motile colloids, *Nature (London)* **503**, 95 (2013).

[20] B. Zhang, H. Yuan, A. Sokolov, M. O. de la Cruz, and A. Snezhko, Polar state reversal in active fluids, *Nat. Phys.* **18**, 154 (2022).

- [21] J. R. Melcher and G. I. Taylor, Electrohydrodynamics: A review of the role of interfacial shear stresses, *Annu. Rev. Fluid Mech.* **1**, 111 (1969).
- [22] D. A. Saville, Electrohydrodynamics: The Taylor-Melcher Leaky Dielectric Model, *Annu. Rev. Fluid Mech.* **29**, 27 (1997).
- [23] D. Das and D. Saintillan, Electrohydrodynamic interaction of spherical particles under quincke rotation, *Phys. Rev. E* **87**, 043014 (2013).
- [24] Y. Hu, P. M. Vlahovska, and M. J. Miksis, Colloidal particle electrorotation in a nonuniform electric field, *Phys. Rev. E* **97**, 013111 (2018).
- [25] Y. Kuramoto, Chemical turbulence, *Chemical Oscillations, Waves, and Turbulence* (Springer, New York, 1984).
- [26] M. A. Schwemmer and T. J. Lewis, The theory of weakly coupled oscillators, *Phase Response Curves in Neuroscience* (Springer, New York, 2012), pp. 3–31.
- [27] T. B. Jones and M. Washizu, Multipolar dielectrophoretic and electrorotation theory, *J. Electrostat.* **37**, 121 (1996).
- [28] S. Kim and S. J. Karrila, *Microhydrodynamics: Principles and Selected Applications* (Dover, New York, 2005).
- [29] M. Kolář and G. Gumbs, Theory for the experimental observation of chaos in a rotating waterwheel, *Phys. Rev. A* **45**, 626 (1992).
- [30] F. Peters, L. Lobry, and E. Lemaire, Experimental observation of Lorenz chaos in the Quincke rotor dynamics, *Chaos* **15**, 013102 (2005).
- [31] I. Hunter, M. M. Norton, B. Chen, C. Simonetti, M. E. Moustaka, J. Touboul, and S. Fraden, Pattern formation in a four-ring reaction-diffusion network with heterogeneity, *Phys. Rev. E* **105**, 024310 (2022).
- [32] See Supplemental Material at <http://link.aps.org/supplemental/10.1103/PhysRevE.107.054603> for (1) derivation of the moment dynamics, (2) comparison of the truncated multipolar model to full numerical simulations, (3) comparison of model predictions and experimental data on Quincke oscillators, (4) examples of other stable attractors, and (5) comparison of numerical and weakly coupled solutions.